References and Notes

1. R. Lakes, *Viscoelastic Materials* (Cambridge Univ. Press, New York, ed. 1, 2009).
2. E. T. Thostenson, C. Li, T. W. Chou, *Compos. Sci. Technol.* **65**, 491 (2005).
3. J. Suhr *et al.*, *Nat. Nanotechnol.* **2**, 417 (2007).
4. A. Cao, P. L. Dickrell, W. G. Sawyer, M. N. Ghasemi-Nejhad, P. M. Ajayan, *Science* **310**, 1307 (2005).
5. X. C. Gui *et al.*, *Adv. Mater.* **22**, 617 (2010).
6. Q. Zhang *et al.*, *J. Phys. D Appl. Phys.* **43**, 315401 (2010).
7. S. Pathak, Z. G. Cambaz, S. R. Kalidindi, J. G. Swadener, Y. Gogotsi, *Carbon* **47**, 1969 (2009).
8. K. Hata *et al.*, *Science* **306**, 1362 (2004).
9. S. Osswald, E. Flahaut, H. Ye, Y. Gogotsi, *Chem. Phys. Lett.* **402**, 422 (2005).
10. Materials and methods are available as supporting material on *Science* Online.
11. M. Zhang, K. R. Atkinson, R. H. Baughman, *Science* **306**, 1358 (2004).
12. L. Qu, L. Dai, M. Stone, Z. Xia, Z. L. Wang, *Science* **322**, 238 (2008).
13. B. Bhushan, X. Ling, A. Jungen, C. Hierold, *Phys. Rev. B* **77**, 165428 (2008).
14. B. Chen *et al.*, *Appl. Phys. Lett.* **83**, 3570 (2003).
15. G. Lenaz, G. Milazzo, *Bioelectrochemistry of Biomacromolecules* (Birkhäuser, Basel, Switzerland, ed. 1, 1997).

16. We acknowledge partial funding by TASC. M.X. acknowledges technical consultations from Y. Hayamizu, A. Izadi-Najafabadi, and Y. Seki.

Supporting Online Material

www.sciencemag.org/cgi/content/full/330/6009/1364/DC1
Materials and Methods
Figs. S1 to S9

9 July 2010; accepted 12 October 2010
10.1126/science.1194865

Video-Rate Molecular Imaging in Vivo with Stimulated Raman Scattering

Brian G. Saar,[1]*† Christian W. Freudiger,[1,2]* Jay Reichman,[3] C. Michael Stanley,[3] Gary R. Holtom,[1] X. Sunney Xie[1]‡

Optical imaging in vivo with molecular specificity is important in biomedicine because of its high spatial resolution and sensitivity compared with magnetic resonance imaging. Stimulated Raman scattering (SRS) microscopy allows highly sensitive optical imaging based on vibrational spectroscopy without adding toxic or perturbative labels. However, SRS imaging in living animals and humans has not been feasible because light cannot be collected through thick tissues, and motion-blur arises from slow imaging based on backscattered light. In this work, we enable in vivo SRS imaging by substantially enhancing the collection of the backscattered signal and increasing the imaging speed by three orders of magnitude to video rate. This approach allows label-free in vivo imaging of water, lipid, and protein in skin and mapping of penetration pathways of topically applied drugs in mice and humans.

Optical imaging techniques are complementary to magnetic resonance imaging (MRI) for in vivo applications. Although the penetration depth of MRI is much higher, optical techniques offer superior spatiotemporal resolution. Label-free optical imaging techniques for in vivo application to humans are attractive because dyes or fluorescent labels may be toxic or perturbative. Recent developments in applying two-photon autofluorescence microscopy (*1*) or second harmonic generation microendoscopy (*2*) in vivo in humans have revealed a wealth of structural and functional information that cannot be obtained with other methods, but those techniques are limited to relatively few specific molecular signatures. Raman spectroscopy offers label-free contrast based on characteristic vibrational frequencies for all major chemical species in tissue, such as lipids, water, DNA, and proteins, as well as a variety of small molecules such as drugs or metabolites. Coherent Raman scattering (*3*) methods allow stimulated excitation of coherent motions of vibrational oscillators and can offer vibrational imaging with subcellular spatial resolution and image acquisition speed that is more than four orders of magnitude higher than that of ordinary Raman microscopy.

Coherent anti-Stokes Raman scattering (CARS) (*4*, *5*) has been used for fast imaging of biological samples, primarily with lipid contrast, (*6*, *7*), at speeds up to video rate (*8*). However, CARS suffers from spectral distortion (*9*), limited sensitivity arising from an unwanted nonresonant background (*10*), nonlinear concentration dependence (*11*), and coherent image artifacts (*12*) that make quantitative interpretation and applications beyond lipid imaging difficult.

The recent development of stimulated Raman scattering (SRS) microscopy overcame these limitations (*13*–*16*) and provided better vibrational contrast (*17*, *18*). In SRS microscopy, the sample is excited by colinear and tightly focused pump and Stokes beams at ω_p and ω_S, respectively. If the difference in frequency ($\Delta\omega = \omega_p - \omega_S$) matches a molecular vibration in the sample at the frequency Ω_{vib} (Fig. 1, A and B), the Stokes beam intensity increases and the pump beam intensity decreases as a result of the coherent excitation of molecular vibrations. When using biocompatible excitation, the intensity changes (ΔI) of the beams are small compared with their intensities ($\Delta I/I < 10^{-3}$). We used a high-frequency modulation transfer method to detect the signal (fig. S1) (*14*, *19*). In this approach, we modulated the intensity of the Stokes beam with an electro-optic modulator and measured the modulation transfer to the pump beam with a lock-in amplifier (LIA) after blocking the modulated Stokes beam with an optical filter. Because laser intensity fluctuations and variations in sample transmission associated with raster scanning the focus through a turbid sample occur at low frequencies, high-frequency detection (>1 MHz) offers superior sensitivity ($\Delta I/I < 10^{-8}$ in 1 s).

Despite the advantages of SRS contrast, it has not been applied in living animals or humans for two reasons: First, previous SRS images required ~1 min per frame, which is much too slow because living animals and humans inevitably move on the microscopic scale (movie S1). To achieve high-speed imaging (Fig. 1C), we modulated the intensity of the Stokes beam at 20 MHz and used a home-built, all-analog lock-in amplifier with a response time of ~100 ns (fig. S2). The colinear laser beams were tuned to match a vibrational frequency of interest (Fig. 1B) and raster-scanned across the sample by a resonant galvanometer mirror with a line rate of 8 kHz (100 ns per pixel at 512 × 512 pixels with up to 25 frames/s). The power levels used here were previously used for in vivo imaging, and no photodamage was observed (*8*). Whereas previous SRS microscopy was limited by the 100-μs response time of a commercial lock-in amplifier (SR844, Stanford Research Systems), our new system is three orders of magnitude faster.

Second, SRS microscopy involves measurement of the intensity loss of the transmitted pump beam, which is not feasible in thick, nontransparent samples (for instance, a human arm). We must rely on backscattering of the forward-going signal by tissue. This signal was previously collected by the excitation objective (*14*), which works for samples with extremely high scattering (*18*). However, in biological tissues, the epi-directed signal collected through the objective is too weak for high-speed imaging: Even with >60-s integration time, the signal-to-noise ratio obtained from tissue was poor (*14*).

To quantitatively understand the light collection in epi-SRS, we performed nonsequential ray-tracing simulations (*20*) by simulating the propagation of a large number (10^6) of rays emitted from the focal volume into a bulk medium with user-defined scattering parameters, which is used as a model for tissue (Fig. 1, D and E). Scattering events along a ray's trajectory are modeled probabilistically (*21*), and we measured the final distribution of the light after it is emitted from the simulated tissue volume. We found that, as expected, 40 to 45% of the light is backscattered in a thick tissue sample because scattering dominates over absorption in most tissues (*22*). Because of multiple scattering, the diffuse cloud of backscattered light has a radius of ~5 mm at the front aperture of the objective lens (Fig. 1F), largely independent of the excitation numerical

[1]Department of Chemistry and Chemical Biology, Harvard University, Cambridge, MA 02138, USA. [2]Department of Physics, Harvard University, Cambridge, MA 02138, USA. [3]Chroma Technology, 10 Imtec Lane, Bellows Falls, VT 05101, USA.

*These authors contributed equally to this work.
†Present address: MIT Lincoln Laboratory, 244 Wood Street, Lexington, MA 02420, USA.
‡To whom correspondence should be addressed. E-mail: xie@chemistry.harvard.edu

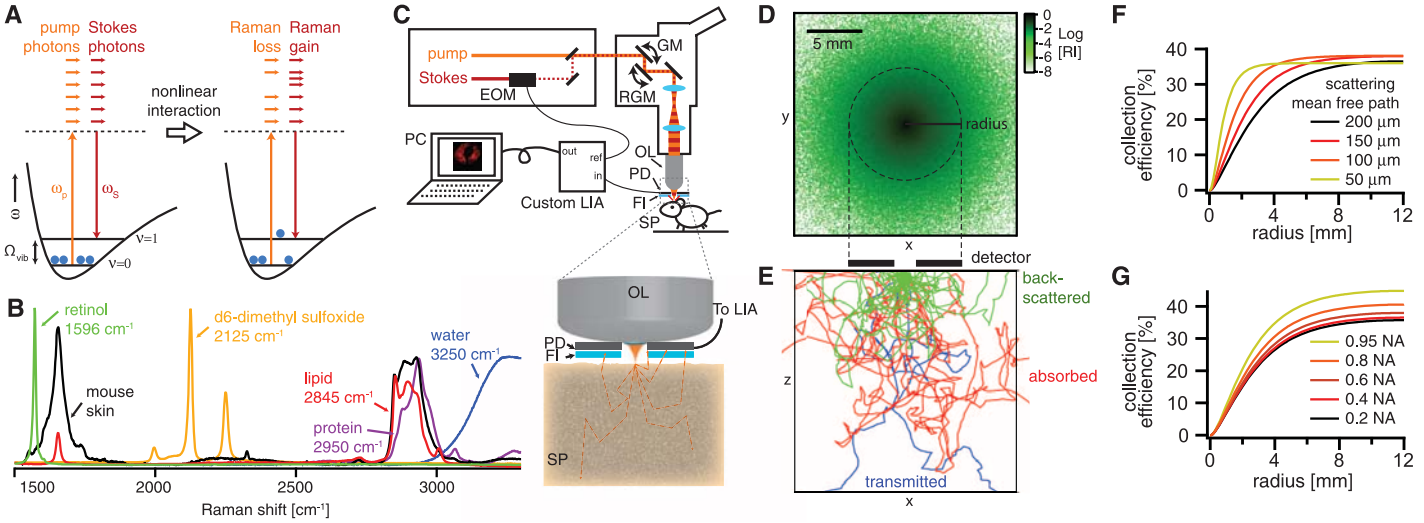

Fig. 1. SRS microscopy. (**A**) Energy diagram of SRS. If the difference frequency of the excitation beams ($\Delta\omega = \omega_p - \omega_S$) matches a vibrational frequency in the sample, Ω_{vib}, a molecule is excited from the vibrational ground state ($v = 0$) to a vibrational excited state ($v = 1$), passing through a virtual state (dashed lines). This results in a photon in the pump field being annihilated (stimulated Raman loss) and a photon in the Stokes field being created (stimulated Raman gain), which can be probed as a contrast for microscopy. (**B**) Raman spectra of chemical compounds imaged in this work. (**C**) Our experimental setup for in vivo SRS microscopy detected the modulation transfer from the Stokes beam to the backscattered pump beam. (Inset) The epi-detector assembly. The specimen (SP) is excited by focusing light with an objective lens (OL) through a small hole in the center of the large-area epi-detector (PD) with a 10-mm outer diameter and a 2-mm aperture in the center. Multiple scattering within the tissue sample redirects a large portion of the forward-traveling light to illuminate the detector active area. The modulated Stokes beam is blocked by an optical filter (FI), and the transmitted pump beam is detected and demodulated by the LIA. Images are constructed by scanning the focal spot in two dimensions with the use of a galvanometer mirror (GM) and resonant galvanometer mirror (RGM). EOM, electro-optic modulator. (**D**) Ray-tracing simulations allow quantitative understanding of the distribution of the relative intensity (RI) of the backscattered light at the tissue surface from a focus at a depth of 100 μm into the tissue (scattering mean free path = 200 μm, anisotropy = 0.9) emitting in the forward direction with a 0.4 numerical aperture. (**E**) Depth profile of tissue showing sample ray trajectories colored according to one of three final outcomes. (**F** and **G**) Simulations of collection efficiency of backscattered, forward-traveling light versus detector radius for (F) different scattering mean free paths of the sample and (G) different numerical apertures (NA) of the excitation objective.

aperture (Fig. 1G). A typical microscope objective has a front-aperture radius of ~1 to 2 mm, so more than 90% of the backscattered light is not collected by the objective, unless it is surrounded by specially-designed parabolic collection mirrors (*23*). We solved this problem by placing the photodetector directly in front of the objective lens and exciting through an aperture in the center of the detector (Fig. 1C). In this geometry, we found in mouse skin that we collected ~28% of the laser light impinging onto the sample. Given the angular distribution of the backscattered light (fig. S3), a filter to block the modulated Stokes beam while transmitting the pump beam had to be specially designed (fig. S4).

Using this system, we imaged skin in vivo in mice. Figure 2 shows single SRS video-rate frames obtained by the CH_2 stretching (primarily lipids; Fig. 2, A and D), OH stretching (primarily water; Fig. 2, B and E), and CH_3 stretching (primarily protein; Fig. 2, F and G) vibrations. The lipid distributions (movie S2) are as expected from previous work (*14*), but water can only be measured in vivo because the skin hydration changes in excised tissue. Imaging water is of particular interest in studying the transport properties of water-soluble drugs and their effect on the hydration of the skin barrier (*24*).

Figure 2C highlights that CARS imaging of water is distorted by the nonresonant background, which introduces an image artifact: It shows a positive contrast "honeycomb" pattern for the lipid-rich areas of the stratum corneum layer, which do not contain water. Thus, the contrast in CARS is inverted compared with the real water distribution.

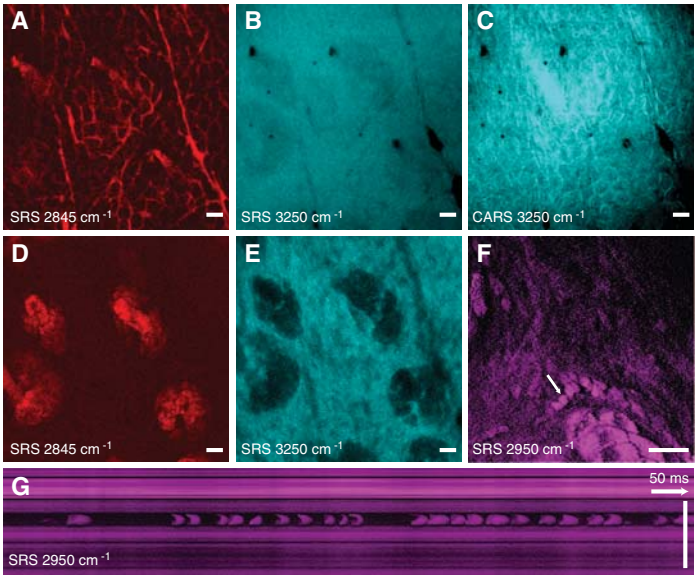

Fig. 2. SRS skin imaging in living mice. (**A**) SRS image of lipids of the stratum corneum shows intercellular spaces between hexagonal corneocytes; (**B**) SRS water image (3250 cm^{-1}) of the same region shows a homogenous distribution of water. (**C**) CARS water image acquired simultaneously with (B) shows artifacts from the nonresonant background of lipids. (**D**) SRS lipid and (**E**) water images of the viable epidermis show sebaceous glands with positive and negative contrast, respectively. (**F**) SRS images of the viable epidermis at the CH_3 stretching vibration (2950 cm^{-1}) mainly highlight proteins, as well as residual lipid-rich structures. A capillary with individual red blood cells (arrow) is visible. The cells are imaged without motion blur due to video-rate acquisition speed. (**G**) SRS in vivo flow cytometry. An x-t plot acquired by line-scanning across a capillary at the position of the arrow in (F) is shown. Individual red blood cells are captured on the fly. Images in (A) to (E) are acquired in epi-direction, whereas those in (F) and (G) are acquired in transmission, all with 37-ms-per-frame acquisition speed and 512 × 512 pixel sampling. Scale bars, 25 μm. The Raman spectra are shown in Fig. 1B.

This effect is not observed in SRS because it is free from this nonresonant background (*14*). Signal averaging can further improve the signal-to-noise ratio if the sample remains still enough (fig. S5).

The protein images (Fig. 2, F and G, and fig. S6) show red blood cells moving in a capillary of the viable epidermis (movie S3), due primarily to the contrast of CH_3 oscillators in hemoglobin. By performing line scans versus time, we reconstructed a plot of the cells as they pass through the scan line (Fig. 2G), allowing for in vivo flow cytometry (*25*) based on intrinsic chemical contrast.

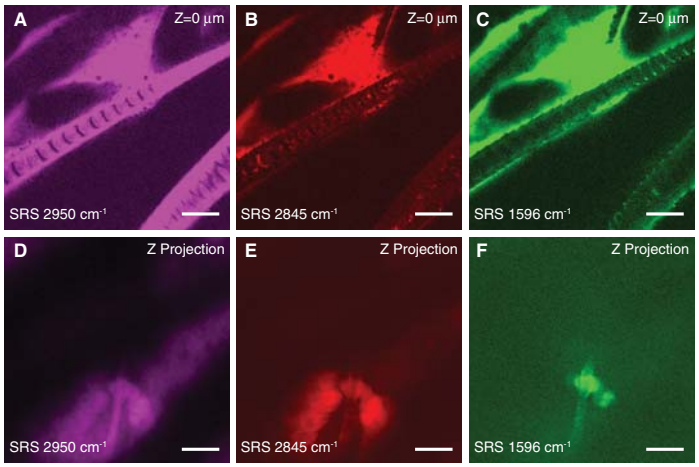

Fig. 3. In vivo imaging of drug penetration of *trans*-retinol. (**A** to **C**) SRS images of hair and stratum corneum in the ear of a living mouse. (**D** to **F**) Depth projection of 3D image stacks of the viable epidermis. Images are acquired at the indicated Raman shifts. Contrast coming primarily from protein (2950 cm^{-1}) and lipid (2845 cm^{-1}) shows the morphology of the skin with all its structural elements and subcellular resolution [see nuclei in (E)]. Nuclei are visible as dark structures in the 2845 cm^{-1} image (E), because the nuclei have low concentrations of lipids. Hairs are visible as solid, periodic structures in the protein image (D) and are surrounded by oil secreted from the sebaceous glands in the lipid image (E). We are able to visualize with SRS that drug penetration of the topically applied *trans*-retinol (C) occurs along the hair shaft (F). Images are collected in transmission with 37-ms-per-frame acquisition speed and 512 × 512 pixel sampling. Scale bars, 25 μm. The Raman spectra are shown in Fig. 1B.

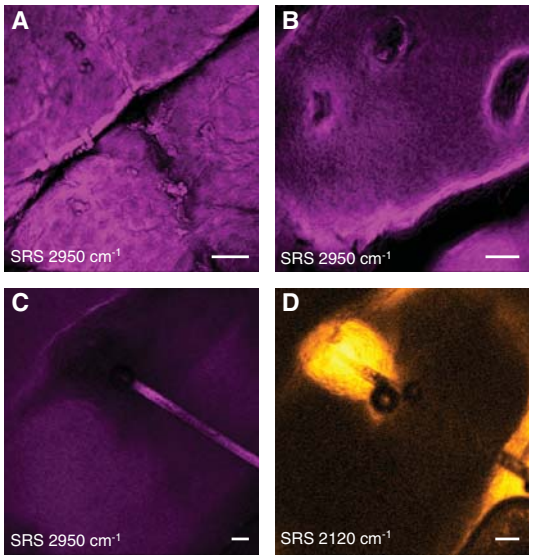

Fig. 4. SRS skin imaging in living humans. (**A** to **C**) SRS images of the stratum corneum and viable epidermis tuned into CH_3 stretching vibration of proteins (2950 cm^{-1}) showing the stratum corneum (A), the viable epidermis (B), and a hair on the skin surface (C). (**D**) SRS image of DMSO penetrating the skin at the same region as shown in (C). We find that DMSO also accumulates in the hair shaft. We used deuterium labeling to create a unique vibration of d6-DMSO at 2120 cm^{-1} for specific imaging. Images are acquired in epi-direction on the forearm of a volunteer (X.S.X.). Image acquisition time is 150 ms for (A) and (B) and 37 ms for (C) and (D), all with 512 × 512 pixel sampling. Scale bars, 50 μm. The Raman spectra are shown in Fig. 1B.

Figure 3 demonstrates the ability of SRS microscopy to follow the penetration of a small-molecule drug (*trans*-retinol, which stimulates collagen synthesis) into mouse skin. Contrast using the CH_3 and CH_2 stretching highlights the morphology of the skin. By tuning in to the polyene stretch of *trans*-retinol, we see that the drug has penetrated via the hair shaft into the sebaceous gland, one of three hypothesized penetration routes into skin (*26*, *27*). Averaging the three-dimensional (3D) data (movie S4), we see the localization of *trans*-retinol surrounding the hair and in the top of the sebaceous gland (Fig. 3F). In our previous work, performed excised tissue, we did not observe this pathway for this drug (*14*), indicating the importance of in vivo studies, because the transport properties of small molecules can be affected by the skin temperature, moisture content, and other factors.

Figure 4 shows in vivo SRS imaging of human skin. Cell layers of the viable epidermis up to a depth of 50 μm can be seen when tuned in to the CH_3 stretching band. High contrast is available for nuclei (Fig. 4, A and B), and the varying nuclear size can be used to find the boundary between the viable epidermis and the stratum corneum. Figure 4C shows a hair disappearing down the hair shaft. In this case, deuterated dimethyl sulfoxide (DMSO), a penetration-enhancing small molecule, was applied to the skin. By tuning to the C-D stretching vibration at 2125 cm^{-1}, contrast from DMSO appeared. DMSO can again be found to accumulate in the area surrounding the hair, though it does not completely penetrate into the hair itself. Such mechanistic insight into the transport of small molecules can only be obtained with label-free chemical imaging.

By overcoming the challenges associated with performing high-speed, epi-detected SRS microscopy, this powerful label-free imaging modality can now be applied to a broad range of problems in whole living organisms, including small animals and humans. The approach presented here can also be applied to other modulation transfer imaging techniques, including two-color two-photon absorption, pump-probe (*28*), and stimulated emission (*29*) microscopy. High-speed vibrational imaging is likely to play an increasingly important role in medical diagnostics in humans.

References and Notes

1. K. König *et al.*, *Microsc. Res. Tech.* **70**, 398 (2007).
2. M. E. Llewellyn, R. P. J. Barretto, S. L. Delp, M. J. Schnitzer, *Nature* **454**, 784 (2008).
3. M. D. Levenson, S. S. Kano, *Introduction to Nonlinear Laser Spectroscopy* (Academic Press, San Diego, 1988).
4. A. Zumbusch, G. R. Holtom, X. S. Xie, *Phys. Rev. Lett.* **82**, 4142 (1999).
5. C. L. Evans, X. S. Xie, *Annu. Rev. Anal. Chem.* **1**, 883 (2008).
6. T. B. Huff, J. X. Cheng, *J. Microsc.* **225**, 175 (2007).
7. T. Hellerer *et al.*, *Proc. Natl. Acad. Sci. U.S.A.* **104**, 14658 (2007).
8. C. L. Evans *et al.*, *Proc. Natl. Acad. Sci. U.S.A.* **102**, 16807 (2005).
9. H. A. Rinia, M. Bonn, M. Müller, *J. Phys. Chem. B* **110**, 4472 (2006).
10. F. Ganikhanov, C. L. Evans, B. G. Saar, X. S. Xie, *Opt. Lett.* **31**, 1872 (2006).
11. L. Li, H. Wang, J.-X. Cheng, *Biophys. J.* **89**, 3480 (2005).
12. J. X. Cheng, A. Volkmer, X. S. Xie, *J. Opt. Soc. Am. B* **19**, 1363 (2002).
13. E. Ploetz, S. Laimgruber, S. Berner, W. Zinth, P. Gilch, *Appl. Phys. B* **87**, 389 (2007).
14. C. W. Freudiger *et al.*, *Science* **322**, 1857 (2008).
15. Y. Ozeki, F. Dake, S. Kajiyama, K. Fukui, K. Itoh, *Opt. Exp.* **17**, 3651 (2009).
16. P. Nandakumar, A. Kovalev, A. Volkmer, *New J. Phys.* **11**, 033026 (2009).
17. B. G. Saar *et al.*, *Angew. Chem. Int. Ed.* **49**, 5476 (2010).
18. M. N. Slipchenko *et al.*, *Analyst (London)* **135**, 2613 (2010).
19. Methods, additional results, and movies are available as supporting material on *Science* Online.
20. *Zemax User's Guide* (Zemax Development Corporation, Bellevue, WA, 2010).
21. S. L. Jacques, C. A. Alter, S. A. Prahl, *Lasers Life Sci.* **1**, 309 (1987).
22. W. F. Cheong, S. A. Prahl, A. J. Welch, *IEEE J. Quant. Elec.* **26**, 2166 (1990).
23. C. Combs *et al.*, *J. Microsc.* **228**, 330 (2007).
24. A. V. Rawlings, C. R. Harding, *Dermatol. Ther.* **17** (suppl, 1), 43 (2004).
25. D. A. Sipkins *et al.*, *Nature* **435**, 969 (2005).
26. M. R. Prausnitz, S. Mitragotri, R. Langer, *Nat. Rev. Drug Discov.* **3**, 115 (2004).
27. J. Lademann *et al.*, *Skin Pharm. Phys.* **21**, 150 (2008).
28. D. Fu, T. Ye, T. Matthews, G. Yurtsever, W. Warren, *J. Biomed. Opt.* **12**, 054004 (2007).
29. W. Min *et al.*, *Nature* **461**, 1105 (2009).
30. We thank J. MacArthur for advice on electronics and K. Sherwood, W. Faustino, and X. Zhang for helpful discussions. C.W.F. was supported by a Boehringer Ingelheim Fonds Ph.D. fellowship. This work was supported by the Bill and Melinda Gates Foundation and an NIH T-R01 award (1R01EB010244-01) to X.S.X. Patent applications based on this work have been filed by Harvard Univ. Imaging was performed in accordance with Harvard Univ. Faculty of Arts and Sciences Institutional Animal Care and Use Committee protocol number 29-01.

Supporting Online Material

www.sciencemag.org/cgi/content/full/330/6009/1368/DC1
Methods
Figs. S1 to S6
Movies S1 to S4

1 September 2010; accepted 4 November 2010
10.1126/science.1197236